1992

Thermal Mathematical Modeling of a Multicell Common Pressure Vessel Nickel-Hydrogen Battery

Junbom Kim
Texas A & M University - College Station

T. V. Nguyen
Texas A & M University - College Station

Ralph E. White
University of South Carolina - Columbia, white@cec.sc.edu

Publication Info

Journal of the Electrochemical Society, 1992, pages 2781-2787.

http://dx.doi.org/10.1149/1.2068979
DOI: 10.1149/1.2068979

cal response. This is certainly the case for the above system since the Li_yNiO_x/WO_3 electrochromic cell can be cycled several thousand times with about 50% change in optical transmission.[23]

Some concern could still be addressed to the charge-discharge rates since they directly influence the device's response time. However, for most applications, response times of the order of one or few seconds are appropriate and thus even materials with relatively slow lithium diffusion rates are still acceptable, providing they offer the required optical properties.

Therefore, the first generation rocking chair batteries, proposed in the early eighties as novel lithium, low-rate rechargeable systems capable of offering long cycle life,[3] have indeed found continued interest. So, the old concept does hold. The question is whether the new concepts for rocking chair batteries, proposed as alternatives to high-energy, high-power lithium and nickel-cadmium batteries,[13,14] will eventually find their way in the competitive portable power source market.

Acknowledgments

The author wishes to thank Dr. B. B. Owens of the University of Minnesota for providing data for calculations and for the helpful discussion.

Manuscript submitted Dec. 9, 1991; revised manuscript received June 8, 1992. This was Paper 31 presented at the Phoenix, AZ, Meeting of the Society, Oct. 13-17, 1991.

Università di Roma "La Sapienza," assisted in meeting the publication costs of this article.

REFERENCES

1. M. Armand, in *Materials for Advanced Batteries,* D. W. Murphy, J. Broodhead, and B. C. H. Steele, Editors, p. 145, Plenum Press, New York (1980).
2. F. Bonino, M. Lazzari, L. Peraldo Bicelli, B. Di Pietro, and B. Scrosati, in *Lithium Batteries,* H. V. Venkatasetty, Editor, PV 81-4, p. 255, The Electrochemical Society Softbound Proceedings Series, Pennington, NJ (1981).
3. M. Lazzari and B. Scrosati, *This Journal,* **127,** 773 (1980).
4. B. Di Pietro, M. Patriarca, and B. Scrosati, *J. Power Sources,* **8,** 289 (1982).
5. M. Lazzari and B. Scrosati, U.S. Pat. 4,464,447 (1984).
6. K. W. Semkov and A. F. Sammels, *This Journal,* **134,** 766 (1987).
7. *Polymer Electrolyte Review I,* J. MacCallum and C. A. Vincent, Editors, Elsevier Applied Science Publishers, London (1987).
8. J. J. Auborn and Y. L. Barberio, *This Journal,* **134,** 638 (1987).
9. K. M. Abraham, D. M. Pasquariello, E. B. Willstaed, and G. F. McAndrews, in *Primary and Secondary Ambient Temperature Lithium Batteries,* J. P. Gabano, Z. Takehara, and P. Bro, Editors, PV 88-6, p. 668, The Electrochemical Society Softbound Proceedings Series, Pennington, NJ (1988).
10. C. D. Dessjardine and G. C. MacLean, Abstract 52, p. 74, The Electrochemical Society Extended Abstracts, Vol. 89-2, Hollywood, FL, Oct. 15-20, 1989.
11. F. A. Uribe and A. F. Sammels, in *Materials and Processes for Lithium Batteries,* K. M. Abraham and B. B. Owens, Editors, PV 89-4, p. 201, The Electrochemical Society Softbound Proceedings Series, Pennington, NJ (1989).
12. R. S. MacMillan, Abstract 43, p. 68, The Electrochemical Society Extended Abstracts, Vol. 90-2, Seattle, WA, Oct. 14-19, 1990.
13. T. Nagaura and K. Tazawa, *Prog. Batteries Sol. Cells,* **9,** 20 (1990).
14. J. R. Dahn, U. von Sacken, M. R. Jukow, and H. Al-Janaby, *This Journal,* **137,** 2207 (1991).
15. J. M. Tarascon and D. Guyomard, *ibid.,* **138,** 2864 (1991).
16. R. Fong, U. von Sacken, and J. R. Dahn, *ibid.,* **137,** 2009 (1990).
17. S. M. Slane and E. J. Plichita, U.S. Pat. 4,983,476 (1991).
18. B. Scrosati, Abstract 31, p. 48, The Electrochemical Society Extended Abstracts, Vol. 91-2, Phoenix, AZ, Oct. 13-17, 1991; N. Imanishi, S. Ohashi, Y. Takeda, O. Yamamoto, and M. Inagaki, Abstract 32, p. 49, *ibid.;* M.-E. Bolster, Abstract 33, p. 51, *ibid.;* Y. Matsuda, M. Morita, T. Hanada, and M. Kawaguchi, Abstract 35, p. 55, *ibid.,* D. Guyomard and J. M. Tarascon, Abstract 36, p. 56, *ibid.*
19. D. Aubarch, M. Daroux, P. Faguy, and E. Yeager, *J. Electroanal. Chem.,* **297,** 225 (1991).
20. K. M. Abraham, M. Alamgir, G. S. Jones, and L. L. Wu, Abstract 691, p. 1029, The Electrochemical Society Extended Abstracts, Vol. 91-2, Phoenix, AZ, Oct. 13-17, 1991.
21. S. Passerini, B. Scrosati, A. Gorenstein, A. M. Andersson, and G. C. Granqvist, *This Journal,* **136,** 3394 (1989).
22. S. Passerini, B. Scrosati, and A. Gorenstein, *ibid.,* **137,** 3297 (1990).

Thermal Mathematical Modeling of a Multicell Common Pressure Vessel Nickel-Hydrogen Battery

Junbom Kim,* T. V. Nguyen, and R. E. White****

Center for Electrochemical Engineering, Department of Chemical Engineering, Texas A&M University, College Station, Texas 77843

ABSTRACT

A two-dimensional and time-dependent thermal model of a multicell common pressure vessel (CPV) nickel-hydrogen battery was developed. A finite element solver called PDE/Protran was used to solve this model. The model was used to investigate the effects of various design parameters on the temperature profile within the cell. The results were used to help find a design that will yield an acceptable temperature gradient inside a multicell CPV nickel-hydrogen battery. Steady-state and unsteady-state cases with a constant heat generation rate and a time-dependent heat generation rate were solved.

The advantages of a nickel-hydrogen battery include long cycle life, high energy density, and a tolerance to high rates of overcharge and reversal.[1-3] Disadvantages of high initial cost and high self-discharge rate do not impair its use in satellite applications where life and reliability are paramount.[3] However, the use of the nickel-hydrogen battery in long life, low earth orbit applications requires greater heat rejection capability.[4,5] The heat removal for a nickel-hydrogen cell depends on passive heat rejection by a conduction mechanism. Since cell performance depends on

* Electrochemical Society Student Member.
** Electrochemical Society Active Member.

the temperature profile inside a cell, the temperature gradient within a cell should be maintained within an acceptable level.

An uneven temperature distribution could lead to electrolyte movement from hot to cold regions by evaporation/condensation[1] which would result in electrolyte redistribution and performance differences due to flooding and drying. At the operating conditions of 30% potassium hydroxide electrolyte solution and 10°C vessel wall temperature, a temperature difference of more than 8.4°C is sufficient to cause electrolyte redistribution as a result of the difference in the water vapor pressure.[6,7] Also, localized heat produced by the oxygen recombination reaction might damage the catalyst in the hydrogen electrode[8] if the temperature is too high.

Radiator, heat pipe, and emissivity control paint are applied to the outside surface of the battery vessel to help reduce the temperature gradient inside the cell.[2,5,9-12] However, to ensure that the maximum temperature gradient is within an acceptable range, optimal cell design for heat transfer must be used. Metallic heat fins are employed in these multicell CPV nickel-hydrogen batteries to reduce the temperature gradient inside the battery, which will extend its life.[4]

A mathematical model can be used to develop the design of these cells because the direct temperature measurement at the specific points inside a cell presents some difficulties such as the following. (*i*) The cell can be contaminated by the thermocouple materials inside the cell stack, and consequently affect the cell performance. (*ii*) It is difficult to insert a thermocouple inside a cell encasement.[13] (*iii*) Since the thermocouple consists of metals, it can act as a heat fin causing the temperature reading to be different from the actual value.

The purpose of this paper is to present a thermal model of a multicell CPV nickel-hydrogen battery that can be used to predict dynamic temperature profiles in two spatial dimensions and to understand the effect of cell design parameter changes on temperature behavior inside the cell.

Model Formulation

The cell design of the multicell CPV nickel-hydrogen battery considered here uses the back-to-back nickel electrode stack as shown in Fig. 1. A cell module consists of nine layers (from right to left in Fig. 1): diffusion screen, platinum electrode, separator, nickel electrode, absorber, nickel electrode, separator, platinum electrode, and diffusion screen. This setup is repeated when more than one module is needed to provide the desired capacity as shown in Fig. 2. In the illustrated design, one cell consists of three modules and a schematic of four cells is shown in Fig. 2. A metallic heat fin is located between every two cells.

Inconel 718 is used as the pressure vessel wall material, and copper is used as the heat fin material in most of the

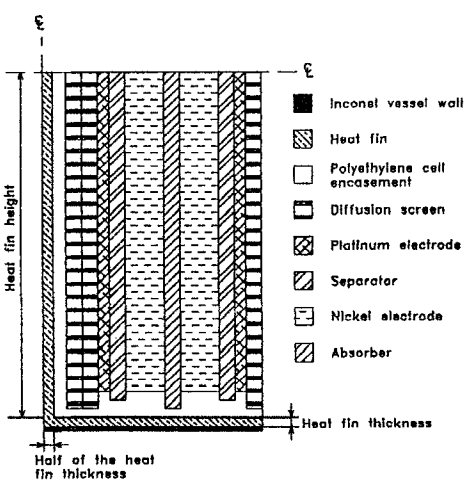

Fig. 1. Schematic representation of the nickel-hydrogen cell module with cell encasement and heat fin.

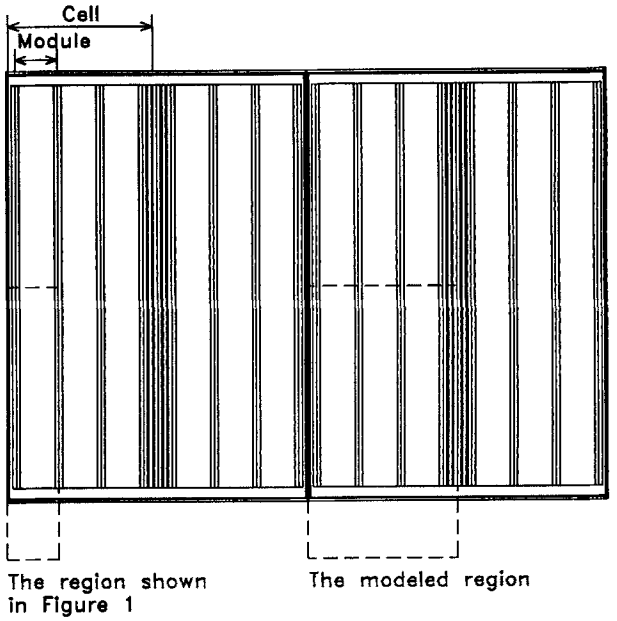

Fig. 2. Schematic representation of the four nickel-hydrogen cell groupings with heat fins and the modeled region.

modeling in this paper except when other material is mentioned. The diffusion screen is made of polypropylene, and its empty region is assumed to be filled with hydrogen gas. Potassium hydroxide solution of 30% concentration is used as the electrolyte, and the porous region of both the nickel and platinum electrodes is assumed to be filled with electrolyte. Asbestos is used as the separator material in these cells, and the porous region of the separator is assumed to be filled with electrolyte. A grafted polypropylene material is used as an absorber material, and the empty region is assumed to be filled with electrolyte. Two polyethylene layers are used for cell encasement.

Heat transfer inside the battery is assumed to occur by conduction. The heat fin is assumed to be in contact with the pressure vessel wall as shown in Fig. 1. A differential energy balance for region i in the cell can be written as follows

$$\rho_i c_{p,i} \frac{\partial T}{\partial t} = \nabla \cdot (\lambda_i \nabla T) + \dot{q}_i \qquad [1]$$

where ρ_i, $c_{p,i}$, λ_i, and $\dot{q}_i$ are the density, specific heat, thermal conductivity, and heat generation rate in region i, respectively. T and t are temperature and time, respectively. It is assumed here that heat is generated uniformly in the nickel electrode layer. The variables considered here are: the number of modules between heat fins, heat generation rate, heat fin geometry (thickness and height), and conductivity of the heat fin. Their effect on temperature distribution and temperature gradient within the cell is presented. The model is used to study the following cases: steady state with constant heat generation rate, unsteady state with constant heat generation rate, and unsteady state with time-dependent heat generation rate case.

A computer software package called PDE/Protran[14] is used to solve Eq. 1 numerically by a finite element method for the modeled region shown in Fig. 2. PDE/Protran solves two spatial dimensions and time dependent partial differential equations. In order to obtain reliable and consistent results, it is necessary to construct smooth and well-dispersed meshes in the modeled region and test the reliability of the aspect ratio. To achieve the desired accuracy (four significant digits), 1500 to 3000 mesh elements are used, depending on the particular problem to be solved.

The height of the heat fin is measured from the top layer of the horizontal part of the fin as shown in Fig. 1. That is, the highest point of the heat fin in the modeled region includes the height of the heat fin, the thickness of the heat fin, and the pressure vessel wall thickness. The thickness of

Table I. Thermal conductivity values of module component structural and filling materials.

Material	Thermal conductivity $\left(\frac{W}{cm \cdot K}\right)$
Polyethylene encasement, λ_m	3.287×10^{-3}
Diffusion screen, λ_m	1.384×10^{-3}
Platinum electrode, λ_m	7.410×10^{-2}
Separator, λ_m	1.443×10^{-3}
Nickel electrode, λ_m	4.256×10^{-1}
Absorber, λ_m	1.384×10^{-3}
30% KOH, λ_f	5.665×10^{-3}
Hydrogen, λ_f	1.722×10^{-3}

the heat fin in the vertical part is half of the heat fin thickness as shown in Fig. 1 because this part is cut in half by symmetry line. The boundary along the left side and right side of the modeled region is assumed to be adiabatic by symmetry because the modeled region is repeated alternately as shown in Fig. 2. The boundary condition of the upper side is also assumed to be adiabatic by symmetry because this line is the centerline of the cell as shown in Fig. 2. The boundary condition for the lower side is set at a constant value because this side is kept at constant temperature by cooling.

The thermal conductivity values of module component structural and filling materials are shown in Table I. The porosity of the diffusion screen, platinum electrode, separator, and absorber are estimated. To investigate the sensitivity of the cell temperature due to the porosity parameter of the above materials, a range of porosity values was assumed into three groups as shown in the parenthesis of Table II. The thermal conductivity values for region i, λ_i, of these groups are calculated with the values in Tables I, II, and Eq. 2, and the results are shown in Table II

$$\lambda = \lambda_m(1 - \varepsilon) + \lambda_f\varepsilon \quad [2]$$

where λ and ε are the thermal conductivity and porosity values, and subscripts, m, f and i represent the values of the structural materials, filling materials, and calculated value with Eq. 2 of region *i*, respectively. The physical and thermal properties of each cell region, such as density, specific heat, and thermal conductivity are calculated using Eq. 2-4 and listed in Table III

$$\rho_i = \rho_m(1 - \varepsilon) + \rho_f\varepsilon \quad [3]$$

$$c_{p,i} = c_{p,m}(1 - \varepsilon) + c_{p,f}\varepsilon \quad [4]$$

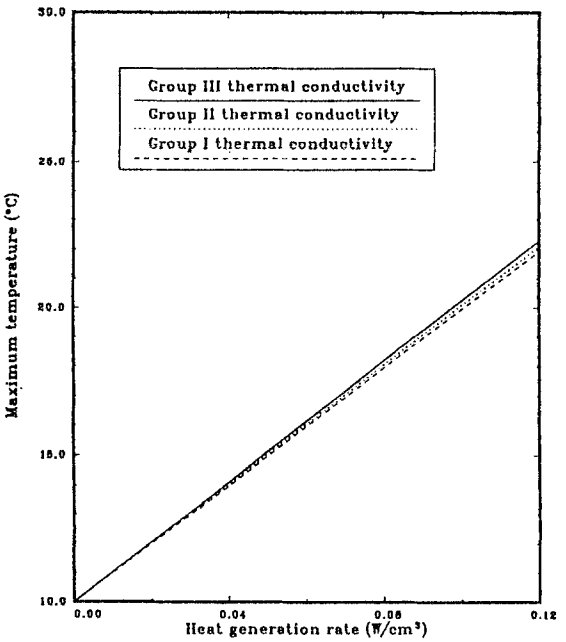

Fig. 3. Comparison of maximum cell temperatures with three different thermal conductivity groups of Table II.

Results and Discussion

The maximum aspect ratio of the element of the modeled region is tested. The maximum cell temperature difference between the two cases, with maximum aspect ratios of 1:15.9 and 1:1.9, is not significant (less than 0.18%). Thus, the former case is used in this modeling work. A constant heat generation rate of 0.04 $\frac{W}{cm^3}$, a copper heat fin of 0.04 cm thickness and 6 cm height, and six modules between heat fins are used on the steady-state modeling case except when other is mentioned.

The effect of component material porosity on maximum temperature is shown in Fig. 3, according to each heat generation rate. As shown in Fig. 3, the effect of porosity on maximum temperature is not significant: the temperature difference between group I and II is 0.06°C (0.43%) and the difference between group II and III is 0.07°C (0.50%) when the heat generation rate is 0.04 $\frac{W}{cm^3}$. Thus, the porosity values of group II could be used in the model without producing a significant error in the temperature profile.

Steady state with constant heat generation rate.—The temperature contour plots of the modeled region are shown

Table II. Three different thermal conductivity groups, λ_i (ε).

Material	I	II	III
Diffusion screen	1.587×10^{-3}(0.6)	1.553×10^{-3}(0.5)	1.519×10^{-3}(0.4)
Platinum electrode	4.673×10^{-2}(0.4)	3.988×10^{-2}(0.5)	3.304×10^{-2}(0.6)
Separator	5.243×10^{-3}(0.9)	4.821×10^{-3}(0.8)	4.398×10^{-3}(0.7)
Nickel electrode	2.546×10^{-1}(0.41)	2.546×10^{-1}(0.41)	2.546×10^{-1}(0.41)
Absorber	5.237×10^{-3}(0.9)	4.809×10^{-3}(0.8)	4.381×10^{-3}(0.7)

Table III. Physical and thermal properties.

Material	Density $\rho_i\left(\frac{g}{cm^3}\right)$	Thermal conductivity $\lambda_i\left(\frac{W}{cm \cdot K}\right)$	Specific heat $c_{p,i}\left(\frac{J}{g \cdot K}\right)$	References
Polyethylene encasement	9.30×10^{-1}	3.287×10^{-3}	2.301	13, 17
Vessel wall	8.166	1.239×10^{-1}	4.602×10^{-1}	13, 17
Copper	8.92	3.849	3.855×10^{-1}	17, 18
Aluminum	2.70	2.109	8.856×10^{-1}	17, 18
Diffusion screen	4.520×10^{-1}	1.553×10^{-3}	8.115	17, 18, 19
Platinum electrode	1.707	3.998×10^{-2}	1.883	17, 18, 20, 21
Separator	1.481	4.821×10^{-3}	2.824	17, 18, 21, 22
Nickel electrode	2.226	2.546×10^{-1}	1.579	17, 18, 20, 21
Absorber	1.171	4.809×10^{-3}	2.999	17, 18, 21

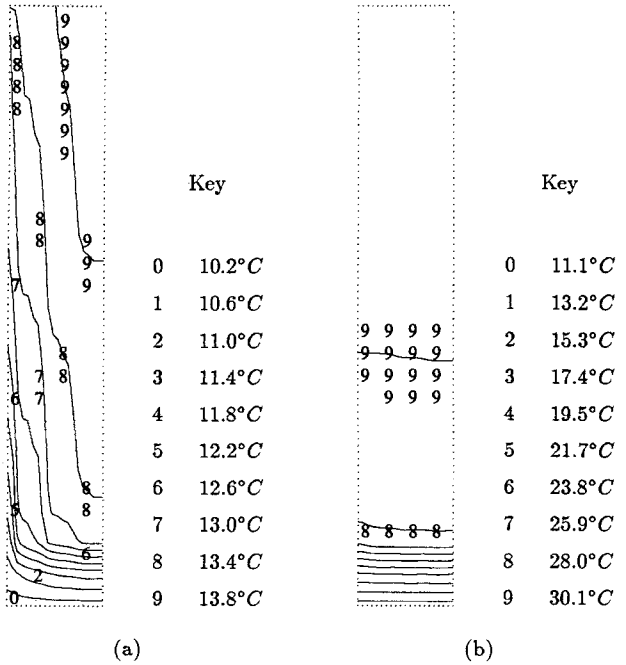

Fig. 4. Temperature contour plots of the modeled region: (a) with heat fin on the left side, (b) without heat fin.

in Fig. 4. The modeled region consists of three modules and a heat fin on the left side as shown in Fig. 2. Figure 4a shows the temperature distribution in the modeled region with a heat fin. The maximum temperature calculated for this case is 14.0°C (4.0°C above the 10°C vessel wall temperature) as shown in Fig. 5. The maximum temperature occurs near the upper right corner, which is the center point of a six module unit. The contour lines 7 and 9 of Fig. 4a show that the temperature gradient is steeper in the horizontal direction (between the modules) than in the vertical direction (along the modules). This demonstrates the utility of the heat fin because the heat generated within the region is dissipated by conduction toward the heat fin and out to the vessel wall through the heat fin. As shown in Table III, the thermal conductivity of the heat fin is one to three orders of magnitude higher than that of other module components.

Figure 4b shows the temperature contour plot of the same modeled region as Fig. 4a for a no heat fin case. The number of the contour lines below line 8 are not shown

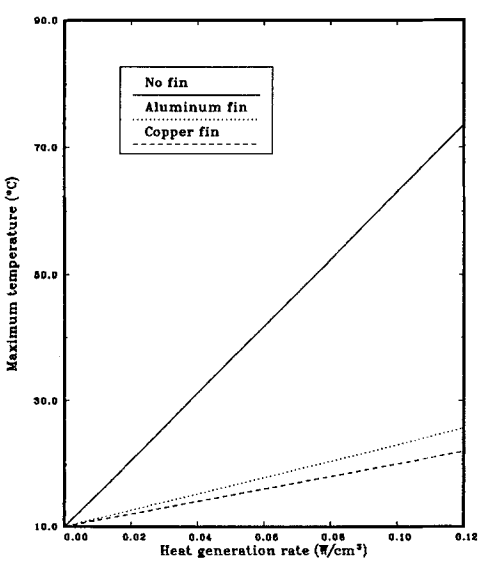

Fig. 5. Comparison of maximum cell temperatures with different heat fin materials.

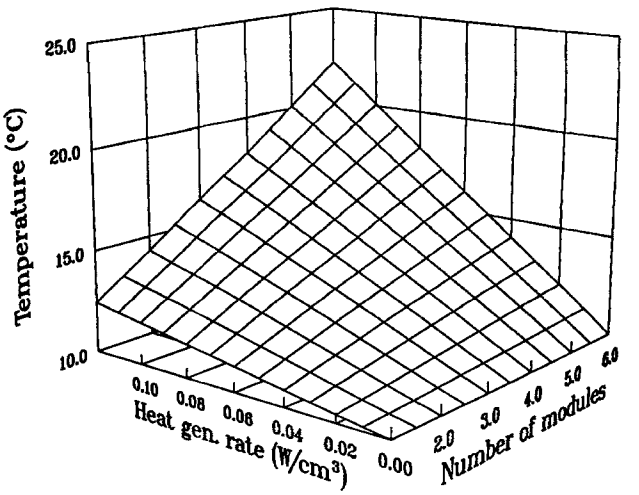

Fig. 6. Comparison of maximum cell temperatures with different heat generation rates and number of modules.

because these lines are too densely stacked. The line numbers decrease one by one such as 7, 6, ···, 0. The temperature gradient and the maximum temperature of Fig. 4b are much steeper and higher than those of Fig. 4a in all of the modeled region. There is a small temperature gradient in the region where the cell components reside; however, beyond this region a large temperature gradient is developed to conduct heat out to the vessel wall. The comparison between the contour plots of Fig. 4a and b explains the definite necessity of having a heat fin inside the cell stack.

A comparison of aluminum and copper heat fins is shown in Fig. 5. As shown in Fig. 5, the maximum temperature in the modeled region without a heat fin is significantly higher at all heat generation rates. Aluminum and copper are comparable as heat fin materials with aluminum offering a small weight advantage and copper providing improved stability. In practice, copper alloy, such as copper beryllium, has also been used due to its superior mechanical properties.

Besides thermal conductivity, there are many aspects to consider in choosing a heat fin material. The heat fin material needs to have good mechanical strength and the ability to sustain its shape and function as a heat path. The weight portion of the heat fin of the entire nickel-hydrogen battery is about 6%, a significant amount that needs to be taken into consideration.[13] Copper is used as the heat fin material in all of the calculations presented below because of its higher conductivity and resistance to corrosion than that of aluminum.

The relation of the maximum temperature in the cell to the heat generation rate and number of modules between heat fins is shown in Fig. 6. Each data point was calculated and combined into a three-dimensional plot. The data points shown in Fig. 6 can be cross checked with those in Fig. 5. As shown in Fig. 6, maximum temperature increases linearly with heat generation rate, and also with the number of modules between heat fins which are repeated with the same pattern.

The relation between maximum temperature and heat fin geometry, such as thickness and height, is shown in Fig. 7. A heat fin of 0.04 cm thickness and 4 cm height is actually 4.04 cm high from the inside vessel wall as shown in Fig. 1. A heat fin height of 0.0 cm line means no heat fin extrusion into the cell stack, although there is a layer equal to the thickness of the heat fin attached along the vessel wall. The maximum temperature decreases from 31.2 to 29.5°C as the thickness is increased from 0.0 to 0.06 cm with a 0 cm fin height. Since the distance from the centerline to the outside vessel wall is fixed, increasing the heat fin thickness means a replacement of the less conductive region of the cell encasement to a more conductive material of copper heat fin. This explains the above observation. The maximum temperature for a fin of 0.01 cm thickness and

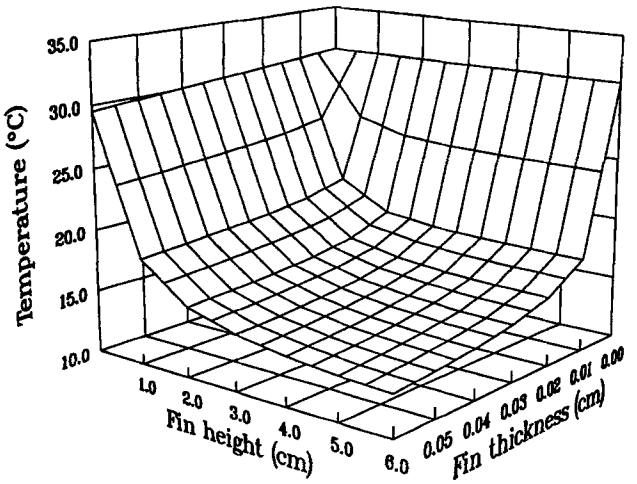

Fig. 7. Comparison of maximum cell temperatures with different heat fin geometries (thickness and height).

2.0 cm height is 18.4°C. Thicker and taller heat fins than the above dimensions yield lower temperatures. Thus, heat fin geometry can be modified to fit each cell design without exceeding the recommended maximum temperature difference ($T_{max} - T_{wall}$) of 8.4°C when a vessel wall temperature of 10°C and 30% potassium hydroxide electrolyte are used.

Unsteady-state with constant heat generation rate.—The maximum temperature in the region as a function of time is shown in Fig. 8, for a constant heat generation rate of 0.04 $\frac{W}{cm^3}$ and copper heat fin size of 0.04 cm thickness and 6 cm height. The steady-state temperatures for each number of modules are shown in Table IV. The three solid lines show the time required to get to 90, 95, and 99% of the steady-state value for each number of modules, respectively. The percent of steady state was calculated based on Eq. 5 given below

$$(\%\text{ of steady state}) = \frac{T - 10°C}{T_{s.s.} - 10°C} \times 100 \qquad [5]$$

where 10°C is the initial temperature in the region and also the temperature of the vessel wall. The time required to get a certain percent of steady-state temperature is linearly proportional to the length of the conductive heat path which is proportional to the number of modules in this model, such that 14 min is required to reach 99% of steady-state value in a one-module case and 59 min is required in a six-modules case.

Table IV. Steady-state temperatures for each number of modules.

Number of modules	1	2	3	4	5	6
Temperature (°C)	10.8	11.4	12.1	12.7	13.4	14.0

Unsteady-state with time-dependent heat generation rate.—Two different heat generation rate curves are shown in Fig. 9.[13] Line a of Fig. 9 is the heat generation rate of a nickel-hydrogen battery of Johnson Controls, Inc., at the beginning of life, and line b of Fig. 9 is that of end of life. The heat generation rate line b of Fig. 9 is less endothermic during the negative heat generation rate region and more exothermic during most of the positive heat generation rate region than that of line a of Fig. 9. The unit of the heat generation rate is $\frac{W}{cm^3}$ of the nickel electrode. The volume of the nickel electrode in this battery is 6.04 cm^3. Both curves are based on a 55 min charge and 35 min, 40% depth of discharge low earth orbit regime, and they will be used as the heat generation rate for the unsteady-state time-dependent case.

The cell design used in Fig. 10 and 11 is six modules between the copper heat fins that are 0.036 cm thick and 6.332 cm high. Figure 10 shows the maximum and minimum temperatures, and the temperature difference between the maximum and minimum temperatures for three repeating cycles when the heat generation rate line a of Fig. 9 is used. The temperature gradient which can cause water relocation is the difference between the hottest and coldest points inside the cell. The maximum temperature difference recommended can be obtained by using the curve of the vapor pressure *vs.* temperature plot of 30% potassium hydroxide solution and water. For the case of outside vessel wall temperature of 10°C and 30% potassium hydroxide solution, the maximum temperature difference recommended to avoid water relocation is found to be 8.4°C.[5,7]

The minimum temperature of the cell is 8.5°C at 18 min. However, this low temperature does not show up in second and third cycles because the cell temperatures prior to the charge regime in second and third cycles are higher than that of the first cycle. The maximum temperature is 16.8°C at the end of discharge during the first cycle. The maximum temperatures of the first and second cycles are the same to two digits but that of the second and third are to five digits. This means that after the first cycle the temperature change according to time is almost identical cycle after cycle. The maximum temperature difference inside the cell

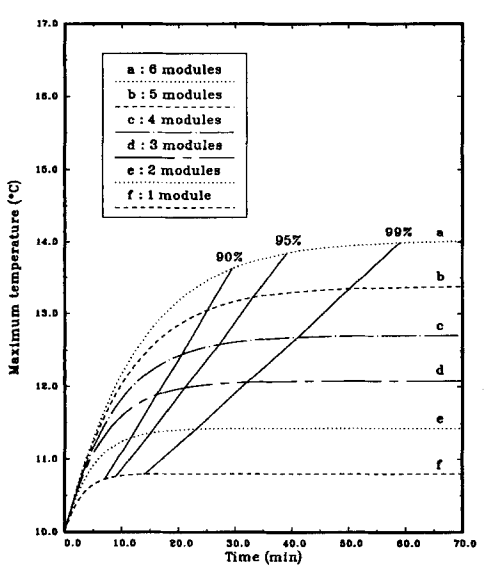

Fig. 8. Maximum cell temperature change for the unsteady-state case using constant heat generation rate.

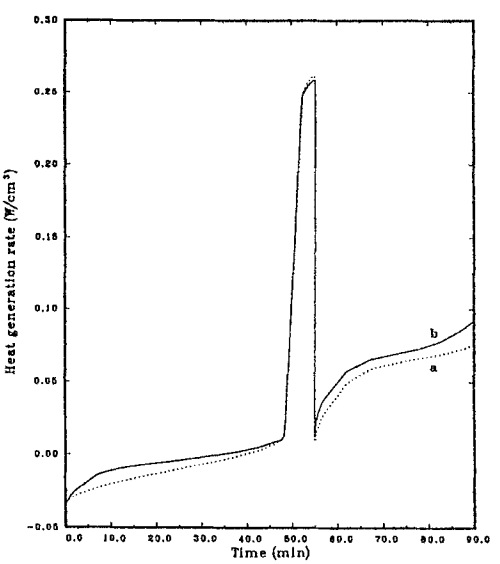

Fig. 9. Time-dependent heat-generation rate of a nickel-hydrogen battery of Johnson Controls, Inc., (a) at the beginning of life, (b) at the end of life.

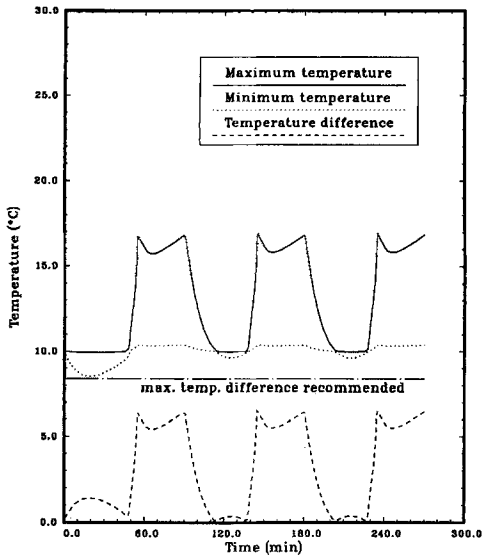

Fig. 10. Temperature change during three cycles with heat generation rate line a of Fig. 9.

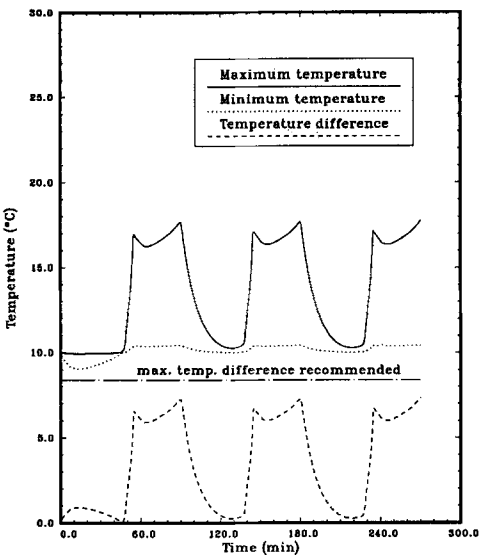

Fig. 11. Temperature change during three cycles with heat generation rate line b of Fig. 9.

is 6.5°C at the end of charge, well below the recommended temperature difference of 8.4°C.

Figure 11 shows the result for the case which uses the heat generation rate line b of Fig. 9. The minimum temperature of the cell for this case is 9.1°C at 13 min which is higher than that of Fig. 10. However, a similar trend of temperature changes cycle after cycle is observed here. The maximum temperature at the end of discharge for the second and third cycle is 17.8°C. The maximum temperature difference inside the cell is 7.3°C at the end of discharge, not exceeding the recommended temperature difference of 8.4°C.

Conclusions

As pointed out in the introduction, it would be difficult to measure the temperature at a specific point inside a cell. Mathematical modeling can help determine how changes in cell design parameters will influence the temperature behavior inside a multicell CPV nickel-hydrogen battery. Thus, a two-dimensional and time-dependent thermal model was developed and presented here.

The effect of the porosity of the diffusion screen, platinum electrode, separator, and absorber on the maximum temperature is found to be insignificant. Comparison of contour plots between cells with and without a heat fin shows a definite necessity for a heat fin to reduce the temperature gradient inside the cell and avoid the possibility of electrolyte redistribution. Two heat fin materials, copper and aluminum, are compared, and copper shows better results. The maximum temperature inside the cell is found to be linearly proportional to the number of modules between the heat fins and the heat generation rate.

It is found that for the configuration investigated here 59 min are needed to reach 99% of the steady-state temperature. The temperature difference between the hottest and coldest points inside a cell is considered to avoid water relocation. A copper heat fin can keep the temperature difference inside the cell below 8.4°C when heat fins of 0.036 cm thickness and 6.332 cm height, six modules between heat fins, and the heat generation rate line a of Fig. 9 are used for calculation. The model could be modified to investigate the temperature behavior of different cell geometries and different thermal and physical values of cell component materials.

Acknowledgments

The authors are grateful for the financial support of this work from the NASA Center for Space Power at Texas A&M University. Also, the authors wish to thank J. P. Zagrodnik and B. M. Page at Johnson Controls, Inc., for their suggestions, and J. P. Fellner at Wright-Patterson Air Force Base for supplying useful information.

Manuscript submitted Nov. 18, 1991: revised manuscript received June 10, 1992.

Texas A&M University assisted in meeting the publication costs of this article.

LIST OF SYMBOLS

c_p specific heat, $\frac{J}{g \cdot K}$
$c_{p,f}$ specific heat of filling material of porous region i, $\frac{J}{g \cdot K}$
$c_{p,i}$ specific heat of region i including structural and filling material, $\frac{J}{g \cdot K}$
$c_{p,m}$ specific heat of structural material of porous region i, $\frac{J}{g \cdot K}$
$\dot{q}_i$ heat generation rate of region i, $\frac{W}{cm^3}$
T temperature, °C
$T_{s.s.}$ temperature at steady state, °C
t time, s

Greek

ε porosity
λ thermal conductivity, $\frac{W}{cm \cdot K}$
λ_f thermal conductivity of filling material of porous region i, $\frac{W}{cm \cdot K}$
λ_i thermal conductivity of region i including structural and filling material, $\frac{W}{cm \cdot K}$
λ_m thermal conductivity of structural material of porous region i, $\frac{W}{cm \cdot K}$
ρ density, $\frac{g}{cm^3}$
ρ_f density of filling material of porous region i, $\frac{g}{cm^3}$
ρ_i density of region i including structural and filling material, $\frac{g}{cm^3}$
ρ_m density of structural material of porous region i, $\frac{g}{cm^3}$

REFERENCES

1. O. D. Gonzalez-Sanabria, *Proceedings of Intersociety Energy Conversion Engineering Conference,* Vol. 2, 453 (1988).
2. S. J. Stadnick, *ibid.,* **3,** 1897 (1980).
3. D. Linden, *Handbook of Batteries and Fuel Cells,* McGraw-Hill, Inc., New York (1984).
4. J. P. Zagrodnik and K. R. Jones, *Proceedings of Intersociety Energy Conversion Engineering Conference,* Vol. 6, 68 (1991).
5. M. J. Milden and C. C. Badcock, *ibid.,* Vol. 1, 191 (1984).
6. M. Klein and B. S. Baker, *ibid.,* 118 (1974).
7. J. Balej, *International J. Hydrogen Energy,* **10,** 233 (1985).
8. D. W. McKee, *J. Phys. Chem.,* **67,** 841 (1963).
9. C. Bulle and A. Dupuy, NTIS N8928276 (1988).
10. F. Betz, J. Stockel, and A. Gaudet, *Proceedings of In-*

tersociety Energy Conversion Engineering Conference, **1,** 510 (1976).
11. S. N. Simons, B. C. Willhoite, and G. Ommering, NTIS N8924427 (1989).
12. H. H. Rogers, E. Levy, Jr., and S. J. Stadnick, AFAPL-TR-77-90 (1977).
13. J. P. Zagrodnik, Personal communication.
14. "PDE/Protran User's Manual," Ver. 2.0, IMSL, Houston, TX (June 1989).
15. R. B. McLellan and P. L. Sutter, *Acta Metall.,* **32,** 2233 (1984).
16. T. I. Evans and R. E. White, *This Journal,* **136,** 2145 (1989).
17. R. H. Perry and C. H. Chilton, *Chemical Engineers Handbook,* 5th ed., McGraw-Hill, Inc., New York (1973).
18. J. A. Dean, *Lange's Handbook of Chemistry,* 13th ed., McGraw-Hill, Inc., New York (1985).
19. C. A. Schaeffer and G. Thodos, *Ind. Eng. Chem.,* **50,** 1585 (1958).
20. R. L. Kerr, Ph.D. Dissertation, University of Dayton, Dayton, OH (1986).
21. S. U. Falk and A. J. Salkind, *Alkaline Storage Batteries,* John Wiley & Sons, Inc., New York (1969).
22. *CRC Handbook of Chemistry and Physics,* 1st student ed., R. C. Weast, Editor, CRC Press, Inc., Boca Raton, FL (1988).
23. M. Earl and J. Dunlop, *Proceedings of Intersociety Energy Conversion Engineering Conference,* Vol. 3, 1395 (1989).
24. B. Baranowski and T. Skoŝkiewicz, *Acta Phys. Pol.,* **33,** 349 (1968).
25. N. A. Godshall and J. R. Driscoll, *This Journal,* **131,** 2221 (1984).

Effects of Phosphate Ions on Copper Dissolution and Passivation

Maria Drogowska*
Département de Chimie, Université de Sherbrooke, Sherbrooke, Québec, Canada J1K 2R1

Louis Brossard*
Institut de Recherche d'Hydro-Québec (IREQ), Varennes, Québec, Canada J3X 1S1

Hugues Ménard
Département de Chimie, Université de Sherbrooke, Sherbrooke, Québec, Canada J1K 2R1

ABSTRACT

The dissolution and passivation of copper was studied in the presence of phosphate and phosphate + chloride in aqueous solution at pH 8 for temperatures ranging from 5 to 60°C. The copper oxidation current increased with (*i*) the concentration of phosphate ions in chloride-free solutions, (*ii*) the concentration of chloride ions in solution containing phosphate ions, and (*iii*) the temperature in both solutions. Two passivation mechanisms are postulated. Below 30°C, a protective base layer of Cu(II) compounds was formed while between 30 and 60°C a porous layer of a Cu(I) compound was formed first on the electrode surface followed by the growth of Cu(II) passive film. The presence of Cu(II) compound was necessary to slow down the copper dissolution. High [phosphate]/[chloride] ratio was favorable for the formation of a thin, compact, passive layer while a high [chloride]/[phosphate] ratio led to the precipitation of a thick porous protective deposit on the copper surface.

The anodic behavior of copper in alkaline solutions has been intensively investigated and numerous publications deal with the subject.[1-12] There exists a general agreement that the anodic layers on copper present a simple Cu_2O or a duplex Cu_2O/CuO, $Cu(OH)_2$ structure depending on electrode potential. The passive film of Cu(II) compounds has a double structure: a lower layer grown via a solid-state mechanism, and an upper layer formed by nucleation and growth from the solution.[1-4,6] $Cu(OH)_2$ is unstable with respect to CuO[15,16] and dehydrates to the oxide for $T \geq 40$°C.

Ions, basic and acidic buffers, and other species present in the solution have different effects on the anodic reactions of copper,[11,12] and it is apparent that they participate in the reactions involving dissolution of metal and passive film formation. Each ion plays a different role depending on the electrode potential. They influence the film's physical and chemical properties, even if they are not detectable in the surface layer.[11-14]

Phosphate is an inorganic anodic corrosion inhibitor acting as a buffering agent. In the presence of phosphate ions, in either alkaline or neutral solutions, the dissolution of copper is sufficiently slowed down in order to allow for passivation.[17] In the case of iron, phosphate is an effective inhibitor only in the presence of oxygen.[18]

In the present study, the behavior of a copper electrode in phosphate and phosphate + chloride deaerated aqueous solutions at pH 8 has been investigated. Various electrochemical techniques were used. Further experiments involving a number of variables, *e.g.*, upper and lower potential sweep limit, sweep rate, or solution concentration and temperature, were also carried out. The electrode surface was examined by optical and scanning electron microscopy (SEM).

Experimental

The measurements were performed in a conventional two-compartment, three-electrode electrochemical cell. The working electrode was either a copper disk electrode rotated at 1000 rpm or a stationary disk electrode (surface area of 0.13 cm^2), cut from a polycrystalline copper rod (Johnson Matthey Chemicals, Ltd., grade 1) and set in a Kel-F holder. Before each experiment, the electrode surface was mechanically polished with an alumina suspension and rinsed with distilled water. At the beginning of each experiment, the copper electrode was immersed in the solution with a potentiostat setting at −0.9 V in order to remove traces of surface oxides.

The auxiliary electrode was a platinum grid separated from the main compartment by a Nafion membrane. A saturated calomel electrode (SCE) connected to the cell by a bridge with a Luggin capillary served as the reference electrode for all potentials quoted in this paper. The resistance of the solution was measured by the ac impedance technique, and the potential was corrected for IR drop.

Each solution was prepared with Baker analytical grade reagent and deionized water. The investigated solutions

* Electrochemical Society Active Member.